Multiresolution Analysis of Radiative Transfer through Inhomogeneous Media. Part II: Validation and New Insights

Nicolas Ferlay, Harumi Isaka, Philip Gabriel, Albert Benassi

Multiresolution Analysis of Radiative Transfer through Inhomogeneous Media. Part II: Validation and New Insights

NICOLAS FERLAY AND HARUMI ISAKA

Laboratoire de Météorologie Physique, Observatoire de Physique du Globe de Clermont-Ferrand, Université Blaise Pascal, Clermont-Ferrand, France

PHILIP GABRIEL

Department of Atmospheric Science, Colorado State University, Fort Collins, Colorado

ALBERT BENASSI

Laboratoire de Météorologie Physique, Observatoire de Physique du Globe de Clermont-Ferrand, Université Blaise Pascal, Clermont-Ferrand, France

(Manuscript received 3 February 2005, in final form 31 August 2005)

ABSTRACT

The multiresolution radiative transfer equations of Part I of this paper are solved numerically for the case of inhomogeneous model clouds using Meyer's basis functions. After analyzing the properties of Meyer's connection coefficients and effective coupling operators (ECOs) for two examples of extinction functions, the present approach is validated by comparisons with Spherical Harmonic Discrete Ordinate Method (SHDOM) and Monte Carlo codes, and a preliminary analysis of the local-scale coupling between the cloud inhomogeneities and the radiance fields is presented. It is demonstrated that the contribution of subpixel-scale cloud inhomogeneities to pixel-scale radiation fields may be very important and that it varies considerably as a function of local cloud inhomogeneities.

1. Introduction

It is well known that radiative transfer plays a key role in many atmospheric processes. In particular, clouds are the major source of uncertainty in global circulation models (Cess et al. 1990) and enter critically in feedback processes that govern the earth's hydrological cycle. In such models, radiative transfer cannot be performed on individual clouds because detailed cloud morphologies are unresolvable. Radiative transfer is also fundamental to the problem of remote sensing, where it is required to determine key cloud properties such as optical depth, drop size distribution, cloud inhomogeneity, and cloud fraction.

Radiative transfer in cloudy atmospheres is a complex problem since the turbulent processes occurring within clouds introduce cloud inhomogeneity that can span a large range of scales (Davis et al. 1996). Although the radiative transfer equation is defined by a linear operator, its solutions are nonlinear with respect to the cloud optical properties. This nonlinear dependence introduces strong scale couplings between the cloud and the radiation fields. Depending on the cloud's morphology, domain-averaged cloud properties may be insufficient to compute fluxes or radiances accurately. In the case of cloud property retrievals, plane-parallel radiative transfer is used, which cannot account for the effects of these scale couplings, and consequently introduces unquantifiable errors in the retrieved cloud parameters (Várnai and Marshak 2001). Taking theses effects into account remains as one of the major issues of remote sensing of inhomogeneous clouds, even though there have been some attempts to evaluate the impact of cloud inhomogeneity on the retrieved cloud parameters (Faure et al. 2001, 2002), or to retrieve means and variances of cloud properties as well as cloud morphological information (Cornet et al. 2004).

In Ferlay and Isaka (2006, hereafter Part I) of this

Corresponding author address: Nicolas Ferlay, Dept. of Atmospheric Science, Colorado State University, Fort Collins, CO 80523.
E-mail: ferlay@atmos.colostate.edu

study, we have developed the multiresolution (MR) radiative transfer equations (RTEs) by applying the multiresolution analysis to the radiative transfer equation. The MR RTEs provide an appropriate framework to study and evaluate scale couplings. In fact, they allow distinguishing pixel-scale radiation sources due to pixel-scale couplings from additional pixel-scale radiation sources due to subpixel-scale couplings. The scale couplings are defined by effective coupling operators (ECOs), the characteristics of which depend on the chosen MR system, connection coefficient matrices, and corresponding scaling and wavelet coefficients of cloud inhomogeneity. While the present approach bears a formal resemblance to those of Stephens (1988b) and Gabriel et al. (1993), which were based on Fourier analysis, it aims to extend them and to gain deeper insights into multiple scale coupling processes.

In Part II of the paper, we demonstrate the feasibility of the MR approach by solving numerically the MR RTEs. Section 2 discusses criteria for choosing a particular MR system and why we used Meyer's system in our numerical computation. We describe also the scale coupling mechanism and its local properties via Meyer's connection matrices and corresponding ECOs for two synthetic clouds: a simple harmonic cloud and a cloud derived from a bounded-cascade model. In section 3, we establish our model's validity by comparing the fluxes and radiances to those calculated using SHDOM (Evans 1998) and Monte Carlo. Then, section 4 provides an analysis of the scale coupling in the radiation fluxes and radiances, with discussions concerning the computed additional radiation sources due to the scale couplings. Section 5 summarizes and concludes.

2. Numerical solution of the MR radiative transfer equations

We will first discuss the choice of the MR system. In doing so, it is important to keep in mind that an MR expansion of a function is considered in the form of partial sum and not in the form of theoretical infinite series (Walter and Shen 2001). We describe the characteristics of Meyer's MR system retained for this study, and the properties of its connection coefficient matrices and corresponding ECOs. Finally we give the other details of the numerical procedure. We assume hereafter that the 1D inhomogeneous cloud and radiance functions are sampled at 2^{J+1} points and approximated in V_{J+1}.

a. The choice of MR system for the MR radiative transfer code

When a function $g(x)$ is approximated in V_{J+1} by using a particular MR system, the accuracy of its MR differentiation depends on the property of translation invariance of the used MR system [see section 3b(2) of Part I]. In fact, approximating $\partial g(x)$ in V_{J+1} with a translation variant MR system leads to neglect of higher order terms that are required for the exact MR differentiation. For Meyer's system, its weak translation invariance requires us only to drop the wavelets at the scale $J + 1$. In contrast, other types of MR systems, such as Haar's and the popular Daubechies' that have finite support in the physical domain and infinite support in the Fourier domain, would require dropping many more terms (McCormick and Wells 1994; Resnikoff and Wells 1998). For Haar's system, the MR discrete differentiation operator is equivalent to the usual centered discrete difference equation $D_J g(x_l) = (1/2\Delta x)[g(x_{l+1}) - g(x_{l-1})]$ with $\Delta x = 2^{-(J+1)}$, which exhibits a severe filtering of the high frequency components. This can modify the spectral characteristic of the radiation fields.

On the other hand, there is a price to pay for translation invariance. The scaling functions associated with translation invariant MR systems, such as Shannon's system, are not in $L^1(\mathbb{R})$ and thus give a poor time or space localization. Fourier expansions are more familiar examples that fall into this category. Good localization in the physical domain is an important and desirable property of MR systems because it can simplify the physical interpretation of scale couplings operating in the MR RTEs. From this point of view, Haar's system has the most desirable characteristic, because its scaling coefficients are directly associated to the arithmetic averaging. However, the main drawback of Haar's system is that the corresponding discrete differentiation operator severely filters the high wavenumber components as discussed above.

Another problem we must consider is the well-known Gibbs phenomenon, associated with expansions of discontinuous functions. The Gibbs phenomenon in MR expansions is discussed by Jerri (1998) and Walter and Shen (2001). It is shown that most of the popular MR systems, including Daubechies' and Meyer's systems, are affected by Gibbs phenomenon, while any MR system with a positive scaling function, such as Haar's system, will not exhibit it.

Since no MR system satisfies all of the desirable properties of space localization, orthogonality, translation invariance, differentiability, and absence of Gibbs phenomenon, we opted to use Meyer's MR system for this study. It can be considered as a good compromise because of its weak translation invariance and the fairly good localization in physical domain of the basis function, although Meyer's expansion is affected by Gibbs phenomenon. However, as will be seen, the results of

radiative transfer through a highly fluctuating bounded cascade cloud show that Gibbs effects are manageable.

With regards to choosing between a periodic and a nonperiodic MR system, we need not assume an implicit periodic cloud domain as in Stephens (1988a) to simulate the radiative transfer through an isolated cloud. Consequently this choice is dictated by the nature of problems we wish to study. Since we prefer to study a periodic cloud domain, we use the periodic version of Meyer's MR system.

b. The characteristics of Meyer's system

Meyer's MR system corresponds to the set of a basis $\{\varphi_{j_0,k_0}, \psi_{j,k}\}$, with $k_0 = 0, \ldots, 2^{j_0} - 1, j = j_{0_\psi}, \ldots, J, k = 0, \ldots, 2^j - 1$. The basis functions are derived from the mother scaling and wavelet functions (see section 3 of Part I), that are defined analytically in Fourier space (Meyer 1990). The scaling function is given by

$$\hat{\varphi}(\omega) = \begin{cases} 1, & \text{if} \quad |\omega| \le 2\pi/3, \\ \cos\left[\dfrac{\pi}{2}\nu\left(\dfrac{3|\omega|}{2\pi} - 1\right)\right], & \text{if} \quad 2\pi/3 \le |\omega| \le 4\pi/3, \\ 0, & \text{elsewhere}, \end{cases} \tag{1}$$

and the mother wavelet by

$$\hat{\psi}(\omega) = \begin{cases} 0, & \text{if} \quad |\omega| \notin [2\pi/3, 8\pi/3], \\ e^{-i\omega/2}\sin\left[\dfrac{\pi}{2}\nu\left(\dfrac{3|\omega|}{2\pi} - 1\right)\right], & \text{if} \quad 2\pi/3 \le |\omega| \le 4\pi/3, \\ e^{-i\omega/2}\cos\left[\dfrac{\pi}{2}\nu\left(\dfrac{3|\omega|}{2\pi} - 1\right)\right], & \text{if} \quad 4\pi/3 \le |\omega| \le 8\pi/3, \end{cases} \tag{2}$$

where $\nu(\xi)$ is the auxiliary function. We use the most frequently used form $\nu(\xi) = \xi^4 (35 - 84\xi + 70\xi^2 - 20\xi^3)$, $\xi \in [0, 1]$. Figures 1a,b show Meyer's functions in physical and Fourier domains. The mother scaling and wavelet functions have compact supports in the wavenumber domain and their supports overlap slightly (Fig. 1b). Consequently, these functions do not have compact support in physical domain (Fig. 1a). However, because $\hat{\varphi}(\omega)$ and $\hat{\psi}(\omega)$ are $C^\infty(\mathbb{R})\varphi(x)$ and $\psi(x)$ are quickly decreasing to zero in the limit $x \to \pm\infty$ at a rate faster than x^{-m}. The function $\varphi(x)$ is centered at zero, and $\psi(x)$ at the abscissa 1/2.

A discrete form of Meyer's MR system, corresponding to the genus of 15, is given by Abry (1996) and used in MATLAB Wavelet toolbox. However we found persistent noise in the spectra of extinction fields; hence we preferred to use the definition of Meyer's system in the Fourier domain, based on local cosine bases as given by Kolaczyk (1994). Accordingly, the MR differentiation for Meyer's system will be defined in the Fourier domain.

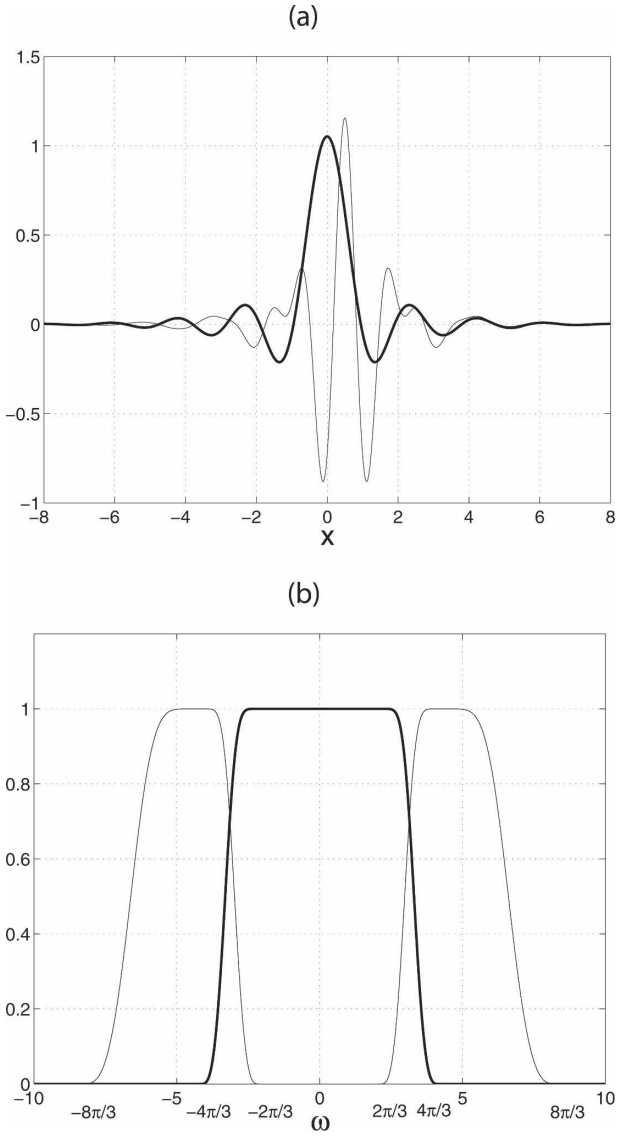

FIG. 1. Characteristics of the mother scaling (thick line) and wavelet (thin line) functions of Meyer's MR system. (a) Their representation if in physical domain; (b) their Fourier transform modulus in the Fourier domain.

c. Properties of the connection coefficients matrices of Meyer's system

As we already noticed in Part I, the connection coefficients for the product contain the information about the mechanisms of scale couplings between radiative

transfer processes and inhomogeneous medium translated in the MR language. Connection coefficients are thus the key components to understanding and computing the scale couplings in radiative transfer. For Meyer's system, understanding the properties of the connection coefficients is simplified in the Fourier domain, where their computation is actually performed. Parseval's formula enables us to rewrite the connection coefficient given by Eq. (21) of Part I, as

$$\langle \chi_{\kappa_1}\chi_{\kappa_2}, \chi_{\kappa_3}\rangle = \frac{1}{2\pi}\int_{\mathbb{R}} \widehat{\chi_{\kappa_1}\chi_{\kappa_2}}(\omega)\,\widehat{\chi_{\kappa_3}}(\omega)\,d\omega, \qquad (3)$$

where $\widehat{\chi_{\kappa_1}\chi_{\kappa_2}}(\omega)$ is the Fourier transform of the product $\chi_{\kappa_1}(x)\chi_{\kappa_2}(x)$. Recall that χ means either φ or ψ, that the subindices κ_i represent in the same time the scale and position indices that define each function of the basis. The index j_0 being fixed, κ_i equals k_0 if $\kappa = \varphi$, and is related to j and k through $\kappa_i = 2^j - 2^{j_0} + k$ if $\kappa = \psi$. We can determine whether a connection coefficient for a given set $\{\kappa_1, \kappa_2, \kappa_3\}$ has a nonzero value by examining the overlapping of the supports of $\widehat{\chi_{\kappa_1}\chi_{\kappa_2}}(\omega)$ and $\widehat{\chi_{\kappa_3}}(\omega)$. Since $\widehat{\chi_{\kappa_1}\chi_{\kappa_2}}(\omega) = \widehat{\chi_{\kappa_1}} * \widehat{\chi_{\kappa_2}}(\omega)$ and the convolution operation tends to widen the Fourier supports of the resulting function, scale couplings will occur at different and nonneighboring scales. Our study thus begins with considerations about support overlap, progressing to a discussion of the effects of the values of integer translations (k_1, k_2, k_3). In what follows, and for the purpose of understanding, we use both notations χ_{κ_1} and χ_{j_1,k_1}. The index j_0 is sometimes denoted j_{0_φ} to make clear that we are dealing with a scaling function.

Let us consider the Fourier supports of $\widehat{\chi_{\kappa_1}\chi_{\kappa_2}}(\omega)$ for the three cases: 1) $\begin{matrix} j_1 = j_{0\varphi} \\ j_2 = j_{0\varphi} \end{matrix}$, 2) $\begin{matrix} j_1 = j_{0\varphi} \\ j_2 = j_\psi \end{matrix}$, and 3) $\begin{matrix} j_1 = j_\psi \\ j_2 = j'_\psi \end{matrix}$ where, by assumption, $j'_\psi \geq j_\psi$. The supports of $\widehat{\chi_{\kappa_1}\chi_{\kappa_2}}(\omega)$ are not given here but can be easily obtained for these three cases. We analyze cases 1 and 3, and then we will discuss case 2 by referring to cases 1 and 3. All numerical examples are computed for $j_0 = 3$ and $J = 6$, and for the periodic version of Meyer's system.

Case 1 corresponds to the coupling between two scaling functions. It is easy to show that the support of $\widehat{\varphi_{\kappa_1}\varphi_{\kappa_2}}(\omega)$ overlaps those of $\widehat{\varphi_{k_3}}(\omega)$ and $\widehat{\psi_{j,k_3}}(\omega)$ for $j \leq j_0 + 1$. Thus, $\langle \varphi_{k_1}\varphi_{k_2}, \varphi_{k_3}\rangle$ and $\langle \varphi_{k_1}\varphi_{k_2}, \varphi_{j,k_3}\rangle$ with $j \leq j_0 + 1$, are nonzero. This implies that the coupling between two scaling functions produces fluctuations described by scaling functions and wavelets at scales j_0 and $j_0 + 1$. The magnitude of this coupling depends on the values of integer translations, as we will see later.

Case 3 corresponds to the coupling between two wavelets. In the general case, the support of $\widehat{\psi_{j_\psi,k_1}\psi_{j'_\psi,k_2}}(\omega)$ is composed of two distinct regions, on positive and negative sides, separated by a gap around $\omega = 0$. It can be shown that the width of this central gap is larger than the width of the support of $\widehat{\varphi_{k_3}}(\omega)$ for $j'_\psi > j_\psi + 2$. This means that $\langle \psi_{j_\psi,k_1}\psi_{j'_\psi,k_2}, \varphi_{k_3}\rangle = 0$ for this condition. When $j_\psi \leq j'_\psi \leq j_\psi + 2$, there is no central gap and $\langle \psi_{j_\psi,k_1}\psi_{j'_\psi,k_2}, \varphi_{k_3}\rangle$ becomes nonzero. The maximum value for $\langle \psi_{j_\psi,k_1}\psi_{j'_\psi,k_2}, \varphi_{k_3}\rangle$ is encountered for the case $j_\psi > j'_\psi$. Thus, the coupling between subpixel fluctuations (especially at the same scale) produces fluctuations at the pixel scale.

Because $\langle \chi_{\kappa_1}\chi_{\kappa_2}, \chi_{\kappa_3}\rangle = \langle \chi_{\kappa_2}\chi_{\kappa_1}, \chi_{\kappa_3}\rangle = \langle \chi_{\kappa_2}\chi_{\kappa_3}, \chi_{\kappa_1}\rangle$, case 2 can be understood by referring to cases 1 and 3. For example, for $\langle \varphi_{k_1}\psi_{j_\psi,k_2}, \psi_{j'_\psi,k_3}\rangle$ and by applying the rules defined above for $\langle \psi_{j_\psi,k_2}\psi_{j'_\psi,k_3}, \varphi_{k_1}\rangle$, we can say that the coupling between a scaling function and a wavelet at the scale j_ψ produces wavelets at the scales j'_ψ satisfying $j_\psi \leq j'_\psi \leq j_\psi + 2$. We interpret this coupling process as a mean of propagating the fluctuations of one field into the second field. [The overlap of the Fourier supports are illustrated for cases 1 and 3 in Figs. 3a,b (case $\Delta k = 0$) presented below.]

Let us examine now how the connection coefficients vary with (k_1, k_2, k_3). The integer translations appear as exponential terms $e^{2-j_1\omega k_1}$, $e^{2-j_2\omega k_2}$, and $e^{2-j_3\omega k_3}$ in Eq. (3). In fact, one can prove easily that the connection coefficients decrease quickly with $x_3 - x_2$ and $x_2 - x_1$, $(x_i)_{i=1,2,3}$ being the center of Meyer's functions $(\gamma_{j_i}, k_i)_{i=1,2,3}$. Figure 2 illustrates this horizontal dependency for the most important coupling processes issued from cases 1–3. Figures 2a,c correspond to the coupling process $\langle \varphi_{k_1}\varphi_{k_2}, \varphi_{k_3}\rangle$ for $j_{0_\varphi} = 3$. Figure 2a gives the norm of the convolution product $|\widehat{\varphi_{\kappa_1}\varphi_{\kappa_2}}(\omega)|$ for different values of the horizontal distance parameter $\Delta k = |k_2 - k_1|$. It shows that the norm decreases as Δk increases. Figure 2c represents $\log |\langle \varphi_{k_1}\varphi_{k_2}, \varphi_{k_3}\rangle|$ for $k_1 = k_3 = 5$, as a function of $k_2 - k_1$. The coefficient is maximum when $k_2 - k_1 = 0$ and then quickly decreases. The curves are almost symmetrical, the slight asymmetry arising from numerical noise. Figures 2b,d are similar to Figs. 2a,c but for the coupling process $\langle \psi_{j_\psi,k_1}\psi_{j'_\psi,k_2}, \varphi_{k_3}\rangle$ and $j_\psi = j'_\psi = 5$: Fig. 2b gives the norm $|\widehat{\varphi_{\kappa_1}\varphi_{\kappa_2}}(\omega)|$ for different Δk, and Fig. 2d represents $\log|\langle \psi_{j_\psi,k_1}\psi_{j'_\psi,k_2}, \varphi_{k_3}\rangle|$ for $k_1 = 17$, $k_3 = 5$, as a function of $k_2 - k_1$. The conclusions are the same as for $\langle \varphi_{k_1}\varphi_{k_2}, \varphi_{k_3}\rangle$: the coupling decreases quickly as the distance $k_2 - k_1$ increases. This last case corresponds to the upscale coupling described above: two wavelets at small scales (here $j_\psi = j'_\psi = 5$) interact to produce a scaling function at the coarse scale $j_{0_\varphi} = 3$.

Let us summarize and interpret the main features of the connection coefficients of the product for Meyer's

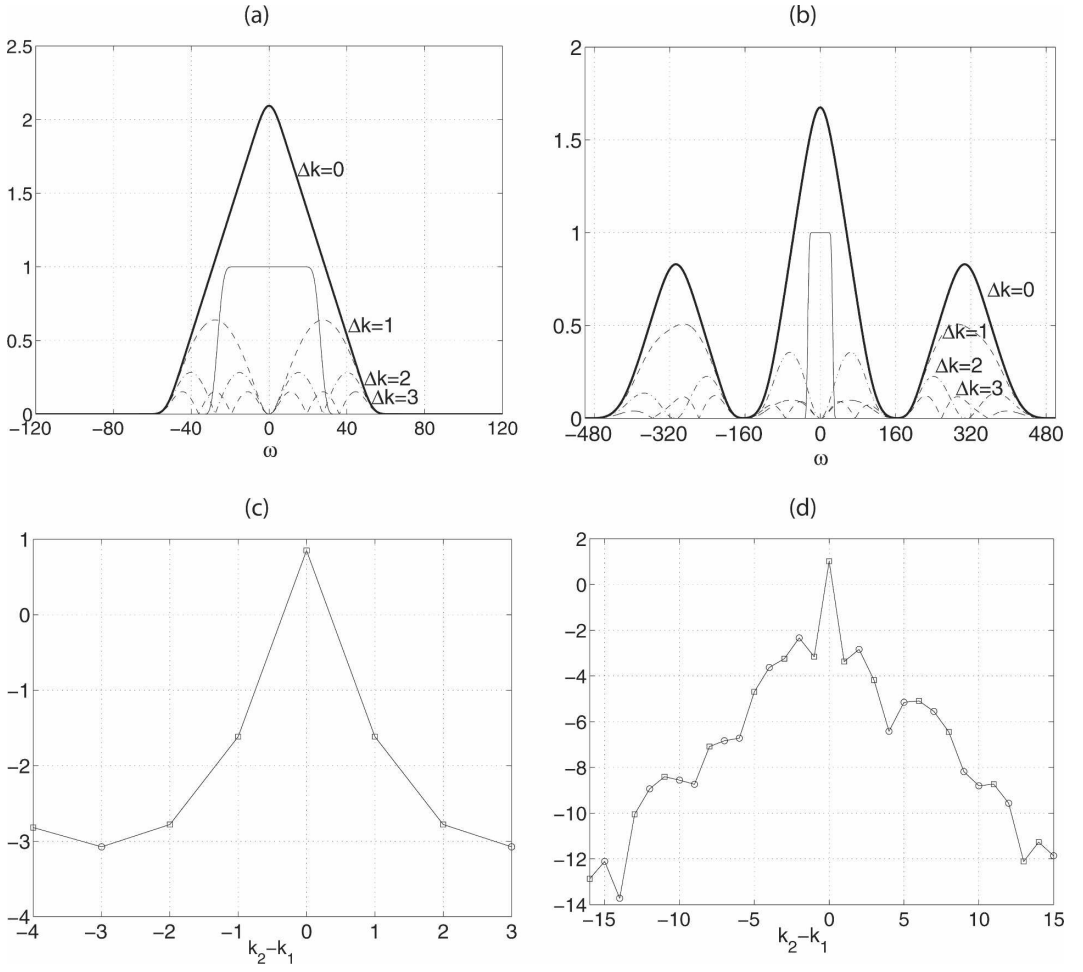

FIG. 2. Illustration of the overlap of Fourier supports and local aspect of the couplings; (a), (b) $|\widehat{\chi_{\kappa_1}\chi_{\kappa_2}}(\omega)|$ for cases 1 and 3, respectively (see text), and for different $\Delta k = |k_2 - k_1|$ [we also plotted $|\widehat{\varphi_{k_3}}(\omega)|$ in thin line]: (a) $|\widehat{\varphi_{\kappa_1}\varphi_{\kappa_2}}|$ with $j_0 = 3$, and (b) $|\widehat{\psi_{j_\psi,k_1}\psi_{j'_\psi,k_2}}(\omega)|$ with $j_\psi = j'_\psi = 5$. (c), (d) The quick decay of the coefficients $\langle\chi_{\kappa_1}\chi_{\kappa_2}, \chi_{\kappa_3}\rangle$ as a function of $k_2 - k_1$: (c) $\langle\varphi_{k_1}\varphi_{k_2}, \varphi_{k_3}\rangle$ with $j_0 = 3$, $k_1 = k_3 = 5$, and (d) $\langle\psi_{j_\psi,k_1}\psi_{j'_\psi,k_2}, \varphi_{k_3}\rangle$ with $j_\psi = j'_\psi = 5$, $k_1 = 17$, $k_3 = 5$ [shown are logarithm of the absolute values of the connection coefficients for the product; markers differentiate positive (□) and negative values (○)].

MR system discussed above. Three fundamental coupling processes are described by the connection coefficients: 1) couplings between two scaling functions to produce another scaling function, that is, pixel-scale coupling, 2) couplings between a scaling function and a wavelet to produce wavelets, and 3) couplings between two wavelets to produce a scaling function. Thus, beside pixel-scale coupling between the cloud and radiation fields (case 1), we can describe a two-step process that projects the effects of the small scales of cloud variability to the coarse scales of the radiation field: first, a coupling between scaling function and wavelets (case 2) creates wavelet components in the radiation field; secondly, the wavelets of the cloud and radiation fields interact (case 3) and generate perturbations of the pixel-scale radiation field. All these couplings keep local characteristics because of their dependency on the integer translations. These fundamental coupling processes are almost independent of the type of MR system; for example the same analysis can be performed using Haar's system.

The magnitude of a coupling is given by the value of the corresponding connection coefficients: the larger the coefficient is in absolute value, the stronger is the associated coupling. Table 1 illustrates the sparsity of $\langle\chi_{\kappa_1}\chi_{\kappa_2}, \chi_{\kappa_3}\rangle$ for the case $j_0 = 3, J + 1 = 7$. The maximum value of $\langle\chi_{\kappa_1}\chi_{\kappa_2}, \chi_{\kappa_3}\rangle$ reaches 2.34 for $\langle\varphi_{k_1}\varphi_{k_2}, \varphi_{k_3}\rangle$, 2.76 for $\langle\psi_{j_\psi,k_1}\psi_{j_\psi,k_2}, \varphi_{k_3}\rangle$ with $j_\psi = 5$, and 2.92 for $j_\psi = 6$. However, only about 30% of the elements exceed 10^{-4} in absolute value, and this percentage decreases to

TABLE 1. Sparsity of $\langle \chi_{\kappa_1} \chi_{\kappa_2}, \chi_{\kappa_3} \rangle$ as a function of different thresholds for Meyer's MR system and $j_0 = 3, J = 6$ (eliminating connection coefficients whose absolute values are less than the threshold).

Threshold	10^{-6}	10^{-5}	10^{-4}	10^{-3}	10^{-2}
Sparsity ε (%)	38.6	57.6	71.4	82.9	92.5

7.5% for a 10^{-2} threshold. These percentages become much smaller as the problem gets bigger (i.e., for a larger J).

The connection coefficient matrix depends only on the choice of the MR system and defines the potentially possible couplings. Whether a coupling is important in a given radiative transfer problem depends on the cloud inhomogeneity. This feature is determined by the ECOs defined in Part I. The number of effective scale couplings may vary significantly with the types of cloud inhomogeneity. Figure 3 illustrates the sparsity of the ECOs for two types of clouds (shown in Fig. 4) and for two thresholds (10^{-3} and 10^{-1}). Figures 3a,b represent the elements of ECOs larger than the thresholds for the sine cloud, and Figs. 3c,d for the bounded cascade (BC) cloud. The difference between the panels shows how the cloud characteristics and the threshold affect the effective scale couplings. The sparsity of the ECOs goes from 70.9% to 90.2% for the sine cloud, and from 38.1% to 82.9% for the BC cloud, as the threshold

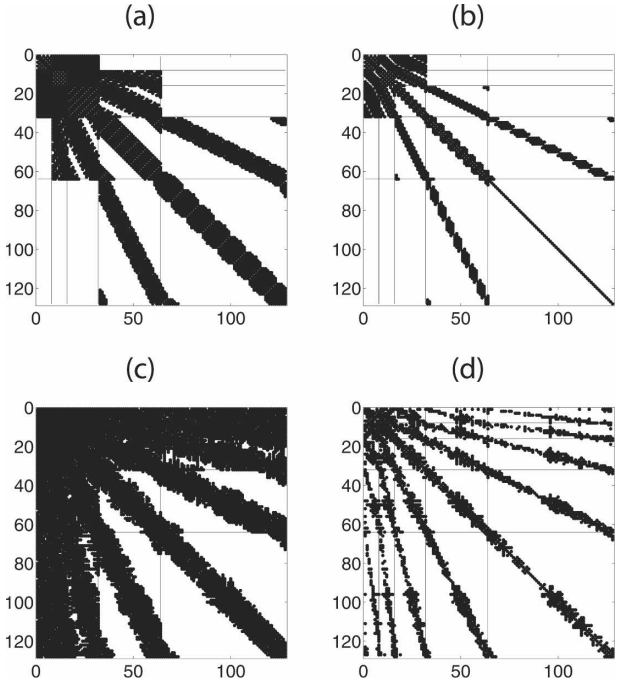

FIG. 3. Standard representation of the ECOs for (a), (b) the sine cloud and (c), (d) the BC cloud. (a), (c) Coefficients larger than 10^{-3} in absolute value; (b), (d) those larger than 10^{-1}.

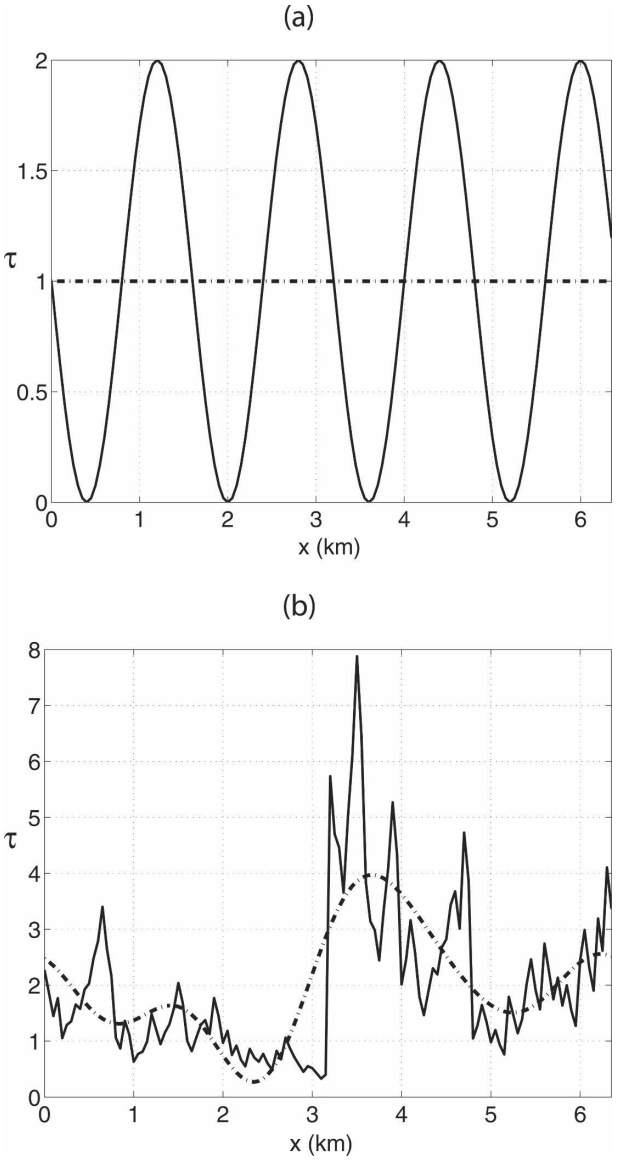

FIG. 4. The two horizontally fluctuating optical thicknesses tested in this study and their low resolution approximations in the sense of Meyer with $j_0 = 3$. Solid line represents the true fluctuations, the dashed–dotted line the approximated fluctuations for (a) the sine cloud and (b) the BC cloud. Clouds are periodic; one period of 6.4 km is shown.

increases. This is because the sine cloud requires only scaling functions and wavelets at the scale $j_0 = 3$ for its representation, while the BC cloud requires scaling functions and all wavelets down to the scale $j_\psi = 6$.

d. Other characteristics of the numerical procedure

1) SOURCE FUNCTIONS

The MR RTEs are obtained by projecting the Fourier amplitude RTE after developing the radiance func-

tion into 2 ($N_F + 1$) Fourier amplitude components. We set $N_F = 32$ in this study, which corresponds to an azimuthal discretization of $\delta\varphi = 12.5°$. A single (Henyey–Greenstein) scattering phase function $P(\mu, \mu')$ is assumed for the entire cloud domain. The internal source functions of the MR RTEs (32) and (34) of Part I are expressed by integrals having the form

$$\int_{-1}^{1} P(\mu, \mu')\left(\widetilde{\boldsymbol{\sigma}^{\varphi/\psi}\mathbf{AI}_n}^{\varphi/\psi}\right)\widetilde{\boldsymbol{N}^{(k-1)}}^{\varphi/\psi}(\mu')\, d\mu'.$$

This integral is transformed into linear weighted sums of integrands at N_q discrete quadrature points $\Sigma_{i=1}^{N_q} w_i P(\mu, \mu_i)(\widetilde{\boldsymbol{\sigma}^{\varphi/\psi}\mathbf{AI}_n}^{\varphi/\psi})\widetilde{\boldsymbol{N}^{(k-1)}}^{\varphi/\psi}(\mu_i)$, and all the necessary modifications should be done to the MR RTEs. After testing both single and double Gauss–Legendre quadratures, we decided to use the single Gauss–Legendre quadrature formula with 16 quadrature points; the zenith angle closest to zero (vertical) is 8.35°, the closest to 90° (horizontal) is 84.55°.

2) Vertical integration: Successive order of scattering

Since the MR RTEs can be cast into a matrix formulation, it would be possible, in principle, to use different numerical methods such as adding–doubling method as in Stephens (1988a). However, in this first attempt to solve the MR RTEs, we preferred to use a simpler approach by approximating the vertical derivative d/dz by its first-order explicit discrete form. The MR RTEs for kth order of scattering are integrated downward from the cloud top to the cloud bottom with the explicit form $F_{i+1} = F_i + (dF/dz)_i\, \delta z$, and then upward from the cloud bottom to the cloud top with $F_i = F_{i+1} - (dF/dz)_{i+1}\, \delta z$. This approach was taken because we wanted to examine how the ratio of the smallest horizontal scale [$\delta x = 2^{-(J+1)}$ domain] to the vertical step (δz) affects the numerical integration, to analyze Gibbs-phenomenon-induced noises propagating away from sharp discontinuities in the optical thickness, and to verify that the horizontal transport of radiation energy due to the horizontal derivatives was accurate. In our simulations, the 0.25 km cloud layer is split into 1000 layers ($\delta z = 25$ cm). This value satisfies a criterion ($\max|\tan\theta| \max|\mathbf{S}^{\varphi\psi}|) \delta z$ domain ≤ 0.2 ($\mathbf{S}^{\varphi\psi}$ is defined in appendix B of Part I), which was found empirically for computational stability for clouds with moderately smooth variations in the optical thickness.

However, for clouds such as bounded cascade cloud with discontinuous variations in their optical thickness, the attenuated direct radiation shows graduate deterioration in accuracy with propagation of Gibbs noise Ultimately, the numerical integration becomes totally unstable. The development of the noises is associated with the horizontal differentiation term, which involves large connection coefficients for first-order differentiation increasing as 2^j, the equivalent of the multiplication of the Fourier transform by the wavenumber in the Fourier domain. This amplifies the high wavenumber noises in the attenuated direct radiation, and finally contaminates all the internal source functions. The $1/\cos\theta$ factor in the horizontal differentiation term also contributes to amplify the noises in radiances for directions close to the horizontal plane. Consequently, we tried to control the development of the noises by imposing a spectral filtering just after the horizontal differentiation step in the numerical integration scheme. This spectral filtering is applied locally to some wavelet coefficients so that the power spectrum of the radiance function does not increase as a function of wavenumber for the last three levels of wavelets ($J - 2 \leq j_\psi \leq J$). For a test cloud exhibiting smooth variation of the optical thickness, spectral filtering is unimportant, while, for clouds exhibiting discontinuous or rapidly extinction fields, this filtering is frequently invoked. We will show below that the noises are not completely suppressed, but kept under control.

3) Other computational issues

Although computational issues are very important in radiative transfer, we don't give here numbers associated with the sizes of matrices and vectors, nor do we indicate the computational complexity, number of operations, or possible exploitation of sparsity of the matrices, etc. The reason is that the numerical results presented are issued from a nonoptimized test code that was written in MATLAB. Our only goal was to test the method in as simple a manner as possible. However, the MR approach can be optimized, for example, by using variable step integration to name one of several strategies. We are presently developing code in FORTRAN language that will exploit the use of sparse matrix-vector multiplication. A future article will give all the details of our new algorithm.

3. Model simulation of shortwave transfer through horizontally inhomogeneous clouds

a. Conditions of test

We present the results obtained for two idealized types of horizontally inhomogeneous and flat-topped clouds with constant vertical profile of extinction coef-

ficient. The two cloud considered are: 1) a sine cloud with a domain-averaged optical thickness of 1 (see Fig. 4a), which provides an example of band limited inhomogeneity; 2) a bounded cascade cloud (denoted hereafter BC cloud) with a domain-averaged optical thickness of 2 (see Fig. 4b), which exhibits a highly fluctuating inhomogeneity. The BC cloud is frequently used in the radiative transfer community (Cahalan 1994; Marshak et al. 1994) because of its interesting properties ($k^{-\alpha}$ spectra where k is the wavenumber, and lognormal distribution of fluctuations). Moreover, the BC cloud used in this study exhibits a central quasi discontinuity that introduces significant numerical difficulties; this allows testing the robustness of the MR radiative transfer code.

The cloud domain extends 6.4 km along the x axis and 0.25 km along the z axis. This cloud domain is periodic along the x axis because of the use of a periodic MR system. The two scale parameters that come with Meyer's MR system are $j_0 = 3$ and $J + 1 = 7$. This means that the extinction field is sampled at 2^7 binary points with an horizontal resolution of $2^{-(J+1)} \times 6.4$ km $= 50$ m, and that the approximation pixels have an horizontal extent of $2^{-j_0} \times 6.4$ km $= 800$ m centered at $k2^{-j_0} \times 6.4$ km, $k = 0, 1, \ldots, 7$, respectively. The analysis of the local upscale couplings will concern how fluctuations of the cloud optical properties at scales from 800 down to 50 m affect the radiation fields at the 800-m approximation pixels. However, it should be noted that the choice of j_0 has no effect on the detailed variations of the MR radiation fields that will be compared to those obtained with SHDOM and Monte Carlo codes.

Uniform collimated radiation illuminates the cloud at a solar zenith angle of 19.17°, which corresponds to the second quadrature point, though it is not required that the zenith angle be equal to a quadrature angle. The surface albedo was set to zero, effectively modeling scenes of thin stratiform clouds above the ocean. The clouds were assumed conservatively scattering ($\varpi = 1$), with an isotropic phase function ($g = 0$). Such a phase function, while not realistic, was used to test the model and simplify our analysis. More realistic (e.g., Mie) phase function can easily be accommodated.

It should be noted that, even if the examples given here are simple and idealized, the model allows the study of much more diverse and realistic conditions. In the MR framework, simulating the actual vertical structure of the cloudy atmosphere means splitting the atmosphere into homogeneous layers and calculating the effective coupling operators for the extinction coefficient variability in each layer. We have tested the MR radiative transfer code for different cloud types (nonflat top, vertically inhomogeneous, larger averaged optical depth), different values of g, etc.

b. Convergence of the MR radiation fields

Since the numerical solution of our MR radiative transfer code is based on successive orders of scattering, a criterion is needed to terminate the computations. For this purpose, we require that the conservation of energy be computed to better than 99%.

Figure 5 shows the evolution of the accumulated normalized fluxes leaving the sine cloud at the outer scale (6.4-km cloud domain) as a function of the order of scattering. The stopping criterion was reached after the 29th order of scattering. Figures 5a,b,c represent downwelling (direct + scattered) and upwelling normalized outgoing fluxes, and their sums (downwelling + upwelling), respectively. In these figures, we plotted three outer-scale fluxes: the first ones due to pixel-scale couplings (denoted $R_{j_0}^{\text{up/down}}$ and in dashed lines), the second ones due to the subpixel couplings (denoted $R_{sub}^{\text{up/down}}$ and in dashed–dotted lines), and the third ones due to all the couplings, which are their sums ($R_{\text{total}}^{\text{up/down}} = R_{j_0}^{\text{up/down}} + R_{\text{sub}}^{\text{up/down}}$ in solid lines). As expected, these fluxes change rapidly within the first ten orders of scattering, and then converge slowly.

The transmission and reflection functions $R_{j_0}^{\text{down}}$ and $R_{j_0}^{\text{up}}$ are equivalent to those we would obtain for the cloud approximated at the scale of scaling functions. The functions R_{sub}^{down} and R_{sub}^{up} converge respectively to -0.044 and $+0.044$ so that the sum of the outgoing fluxes due to subpixel couplings converge to zero (Fig. 5c). Because the media are not absorbing, we must have $R_{j_0}^{\text{down}} + R_{j_0}^{\text{up}} \to 1$, $R_{\text{total}}^{\text{down}} + R_{\text{total}}^{\text{up}} \to 1$ and consequently $R_{\text{sub}}^{\text{down}} + R_{\text{sub}}^{\text{up}} \to 0$. It is crucial to check the radiation budgets of each aforementioned relations to avoid introducing spurious radiation sources in numerical procedure. The discussions in this section point to an important feature: additional sources due to subpixel couplings only change the distribution between the outer-scale reflected and transmitted fluxes.

For the sine cloud, neglecting subpixel couplings lead to underestimating the cloud transmission by 4.4% and overestimating the reflection by the same amount. In the case of the BC cloud, the corresponding fluxes are -0.022 (upwelling) and 0.019 (downwelling): these fluxes do not cancel out completely. This may be due to the high frequency noise, in particular in direct downward flux, generated by Gibbs phenomenon. Moreover, it is quite possible that the calculation is stopped before the scattered fluxes attain locally their convergence, the BC cloud exhibiting much higher optical thicknesses than the sine cloud.

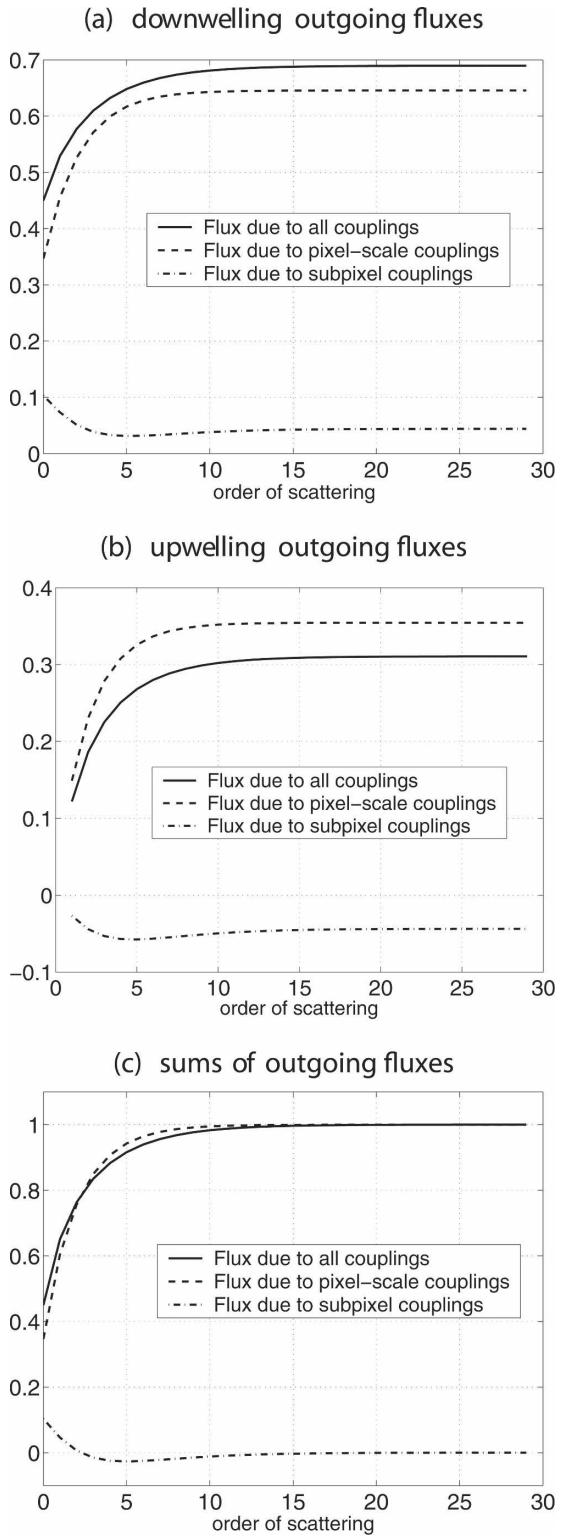

FIG. 5. Evolution with the order of scattering of the normalized accumulated fluxes leaving the sine cloud at the outer scale: (a) downwelling outgoing fluxes; (b) upwelling outgoing fluxes; and (c) their sums (upwelling + downwelling; see text for details).

c. Comparisons of the radiation fields

Before analyzing the scale couplings, we compared first the MR radiative transfer code results, designated hereafter WaveNum, with those calculated using SHDOM (Evans 1998) and Monte Carlo (MC) codes for radiances (for some directions) and fluxes. We used a forward MC code written by Marshak et al. (1995) that obtains efficiency by using the maximum cross-section approach (Marchuk et al. 1980). To attain an average accuracy of less than 1% for radiances, the simulations require 3×10^9 photons (Cahalan et al. 1994b). The results of two types of MC simulations are given: for those designated by MC∞, scattered photons are pursued until their energy becomes less than a negligible threshold, while for those designated by MC29 (or MC26), scattered photons are followed only up to the maximum order of scattering of 29 (26), which is dictated by the requirements of WaveNum. All fluxes and radiances are given below for a normalized incident flux of unity.

1) Comparisons of the radiance fields

(i) Sine cloud

In Fig. 6, we plot upwelling radiances obtained by WaveNum, SHDOM, and MC∞ for two viewing directions: ($\varphi = 0°$, $\theta = 8.35°$) and ($\varphi = 0°$, $\theta = 84.55°$); these two zenith angles correspond to the extreme zenith angles of the eight-point Gauss–Legendre quadrature. MC29 is not plotted because it is indistinguishable from MC∞. In the first direction (Fig. 6a), WaveNum radiances agree quite well with both SHDOM and MC radiances, except that we slightly underestimate the radiance near its maximum. In the second direction (Fig. 6b), WaveNum radiances follow the spatial pattern of the two other radiances, but underestimate them by about 6% over the entire domain. The causes of this underestimate could not be pinned down, but probably involve the simple discretization of d/dz and the slight spectral filtering. The noisy MC radiance in Fig. 6b is due to the small number of photons exiting in the indicated direction.

(ii) BC cloud

In this case of the BC cloud, the conservation of energy to better than 99% is reached after 26th order of scattering. Figure 7a shows upwelling radiances obtained by the different codes for the direction ($\varphi = 0°$, $\theta = 8.35°$). Both MC∞ and MC26 are shown because some significant differences exist between them. Radiances calculated with WaveNum agree quite well with

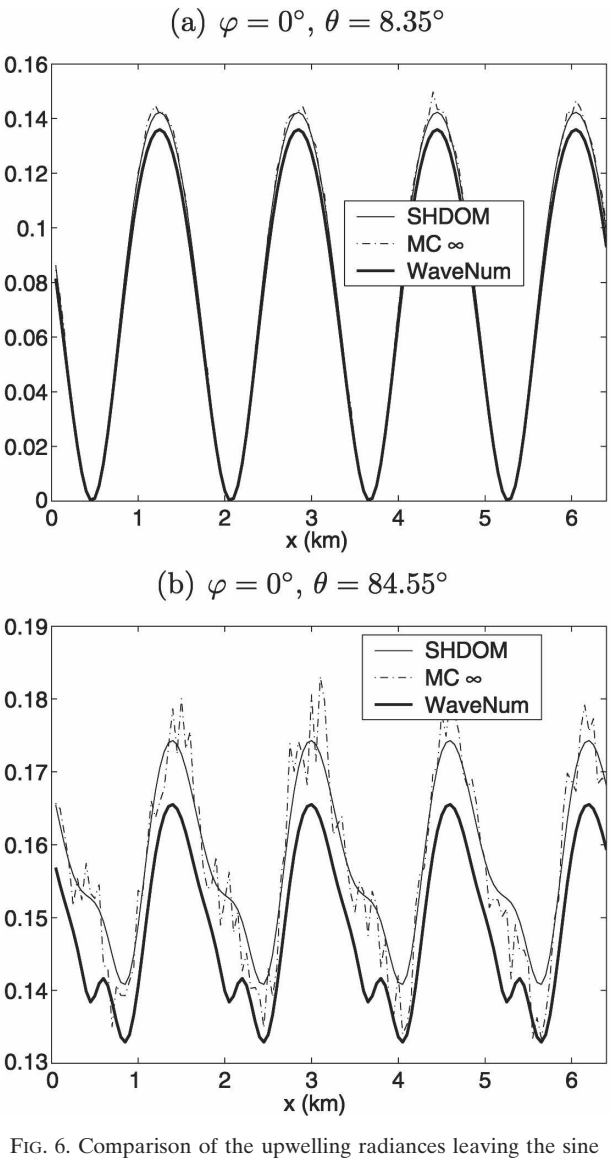

FIG. 6. Comparison of the upwelling radiances leaving the sine cloud in two directions: (a) $\theta = 8.35°$ and (b) $\theta = 84.55°$.

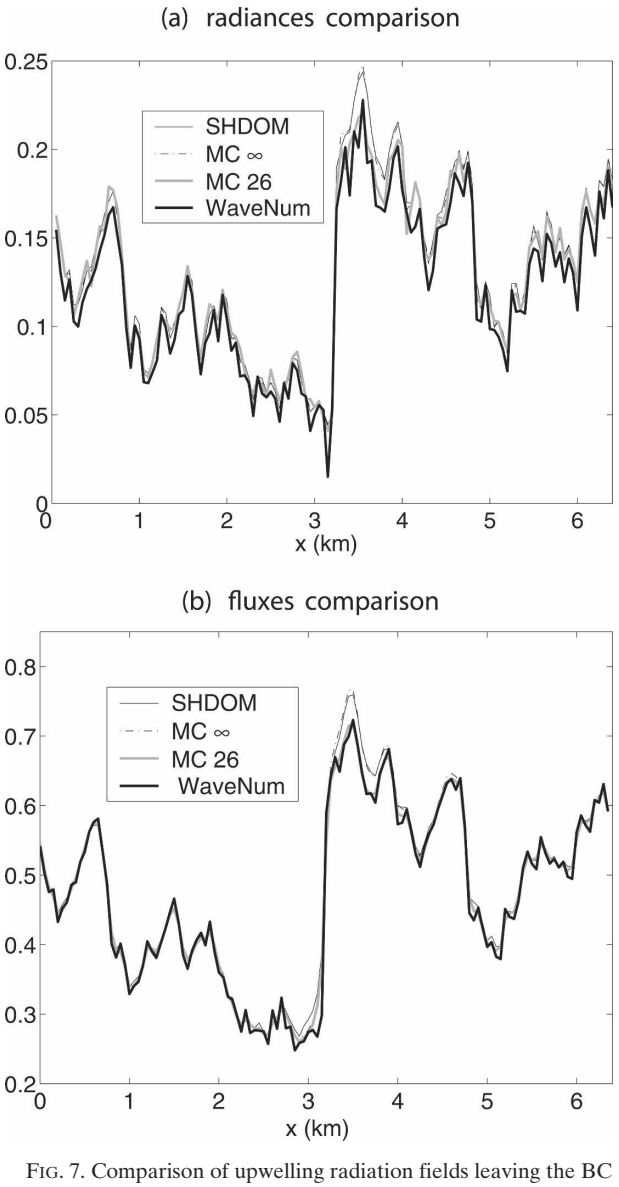

FIG. 7. Comparison of upwelling radiation fields leaving the BC cloud: (a) upwelling radiances in the direction $\varphi = 0°$, $\theta = 8.35°$; (b) upwelling fluxes.

both SHDOM and MC radiances. They tend to follow better the MC26 curve in the right-hand half of the domain where the radiation field has not totally converged after 26th order of scattering. One can observe globally a slight underestimation of the radiances, and some large amplitude noise near the central discontinuity of the extinction field. For nearly horizontal directions (not shown here), WaveNum radiances are more affected by small-scale fluctuations. The BC cloud imposes a severe test for the MR radiative transfer code, because of the presence of Gibbs phenomenon, particularly increased in near-horizontal directions (large $1/\cos\theta$ factor in the horizontal differentiation term). However, WaveNum keeps the Gibbs effects under control in all directions, as proved by the good flux comparison given below.

2) COMPARISONS OF THE RADIATIVE FLUXES

(i) Sine cloud

We will not present here the sine cloud case, because the fluxes obtained with the different codes are very close and hard to distinguish. The absolute errors in WaveNum fluxes relative to those of SHDOM do not exceed 0.0067 for a normalized incident flux of unity. The relative domain averaged errors are 0.063% and 0.016% for the upwelling and downwelling fluxes, respectively.

(ii) BC cloud

Figure 7b gives the upwelling radiative fluxes emerging from the BC cloud, obtained by WaveNum, SHDOM, MC∞ and MC26. As expected from the comparison of the upwelling radiances, the spatial distribution of upwelling fluxes computed by WaveNum while agreeing well with both SHDOM and MC fluxes, is closest to the MC26 curve. The relative error in the domain averaged WaveNum upwelling flux is respectively 1.93% relative to SHDOM and 0.48% relative to MC26. Concerning the comparison of the downwelling fluxes (not shown here), WaveNum is affected by significant fluctuations at the smallest scale, and overestimates the flux at the central discontinuity, the Gibbs phenomenon polluting in particular the collimated direct radiation. In spite of this noise, the relative error in the domain averaged WaveNum downwelling flux is still relatively small: 0.40% relative to SHDOM and 0.44% relative to MC26.

4. Analysis of the scale couplings

We exploit now the MR feature of our radiative transfer simulations. Let us examine again the MR formulation of the multiscale coupling between the radiation and cloud fields expressed principally by Eq. (29) of Part I. The following expressions are its slightly modified version:

$$\widetilde{\sigma N^k}^{\varphi} = \widetilde{\sigma^{\varphi}\mathbf{AI}_n}^{\varphi}\,\widetilde{N^k}^{\varphi} + \left(\widetilde{\sigma^{\psi}\mathbf{CI}_n}^{\varphi}\,\widetilde{N^k}^{\varphi} + \widetilde{\sigma^{\varphi}\mathbf{BI}_n}\,\widetilde{N^k}^{\psi} + \widetilde{\sigma^{\psi}\mathbf{DI}_n}^{\varphi}\,\widetilde{N^k}^{\psi}\right), \tag{4}$$

$$\widetilde{\sigma N^k}^{\psi} = \widetilde{\sigma^{\psi}\mathbf{DI}_n}^{\psi}\,\widetilde{N^k}^{\psi} + \left(\widetilde{\sigma^{\varphi}\mathbf{AI}_n}^{\psi}\,\widetilde{N^k}^{\varphi} + \widetilde{\sigma^{\psi}\mathbf{CI}_n}^{\psi}\,\widetilde{N^k}^{\varphi} + \widetilde{\sigma^{\varphi}\mathbf{BI}_n}\,\widetilde{N^k}^{\psi}\right). \tag{5}$$

These equations involve the different effective coupling operators $\widetilde{\sigma^{\varphi}\mathbf{AI}_n}^{\varphi/\psi}$, $\widetilde{\sigma^{\psi}\mathbf{CI}_n}^{\varphi/\psi}$, $\widetilde{\sigma^{\varphi}\mathbf{BI}_n}^{\varphi/\psi}$, and $\widetilde{\sigma^{\psi}\mathbf{DI}_n}$. The column vectors $\widetilde{\sigma N^k}^{\varphi}$ and $\widetilde{\sigma N^k}^{\psi}$ are vector representations of the scaling and wavelet coefficients of the product $\widetilde{\sigma N^k}$, respectively, that determine the radiation field at the pixel scale and subpixel scales, respectively [see section 4 of Part I for the definition of the terms pixel scale and subpixel scales, and also Eqs. (31) and (33)]. In the discussions below, we will treat $\widetilde{N^k}^{\varphi/\psi}$ as if they represent the associated radiation field itself.

Equation (4) indicates that the scaling coefficients $\widetilde{\sigma N^k}^{\varphi}$ are expressed as the sum of two types of contributions: one due to pixel-scale couplings (the first term), the other (three terms in the parentheses) due to scale couplings. As already discussed in section 4a of Part I, these three terms constitute an additional internal radiation source for the pixel-scale radiation fields. In section 2c above, we have shown that this additional radiation sources results essentially through the coupling term $\widetilde{\sigma^{\psi}\mathbf{DI}_n}^{\varphi}\,\widetilde{N^k}^{\psi}$, that is, the coupling between wavelet-scale fluctuations of both the cloud optical properties and radiation fields, illustrated in Figs. 2b,d.

From the above discussion, the radiation fields at the pixel scale consist of two components: the first, denoted hereafter $R_{j_0}^{\text{up/down}}$, which corresponds to the solution of this equation due only to pixel-scale couplings, and the second one, denoted hereafter $R_{\psi\to j_0}^{\text{up/down}}$, which is the additional pixel-scale radiation field due to scale couplings. This second field $R_{\psi\to j_0}^{\text{up/down}}$ quantifies the magnitude of the errors that would be made in the pixel-scale radiation fields when the cloud is represented approximately with the scaling coefficients σ^{φ}. From this point of view, the sine cloud we tested is particularly interesting because its approximate representation is that of a plane-parallel cloud, as will be seen below.

To summarize and as illustrated in Fig. 2 of Part I, the quantity $R_{j_0}^{\text{up/down}}$ is the consequence of pixel-scale couplings at 800-m scale while $R_{\psi\to j_0}^{\text{up/down}}$ (also at the scale of 800 m) arises from the four scales of cloud subpixel fluctuations, extending from 50 to 800 m. We denote hereafter their sum $R_{\text{total}\,j_0}^{\text{up/down}}$, the unbiased pixel-scale radiation field.

The field $R_{\psi}^{\text{up/down}}$ at the wavelet scales is the solution of the RTE at subpixel scales [Eq. (33) of Part I]. Thus, the entire radiation fields due to scale couplings, denoted as $R_{\text{sub}}^{\text{up/down}}$ in section 3b, can be expressed as $R_{sub}^{\text{up/down}} = R_{\psi\to j_0}^{\text{up/down}} + R_{\psi}^{\text{up/down}}$. Because of the property $\int_{\mathbb{R}} \psi_{j,k}(x)\,dx = 0$, we have $\int_{\mathbb{R}} R_{\psi}^{\text{up/down}}\,dx = 0$, and the cloud domain average of $R_{\text{sub}}^{\text{up/down}}$ is equal to the cloud domain average of $R_{\psi\to j_0}^{\text{up/down}}$.

It is important here to note that the pixel-scale additional quantity $R_{\psi\to j_0}^{\text{up/down}}$ is a correction to the pixel-scale biased quantity $R_{j_0}^{\text{up/down}}$ due to the associated low resolution representation of the cloud field. Hence, $R_{\psi\to j_0}^{\text{up/down}}$ is not a measurable quantity and can be positive or negative. Below, we will sometimes talk about additional negative radiation sources and their propagation.

a. Low resolution representation of the cloud inhomogeneities

The low resolution representations of the two test clouds shown in Fig. 4 (dashed–dotted lines) are reconstructed from eight scaling coefficients $\{\langle\sigma, \varphi_k\rangle, k = 0, \ldots, 2^{j_0} - 1\}$ with Meyer's system and $j_0 = 3$. In both cases, the small-scale fluctuations are not obviously in-

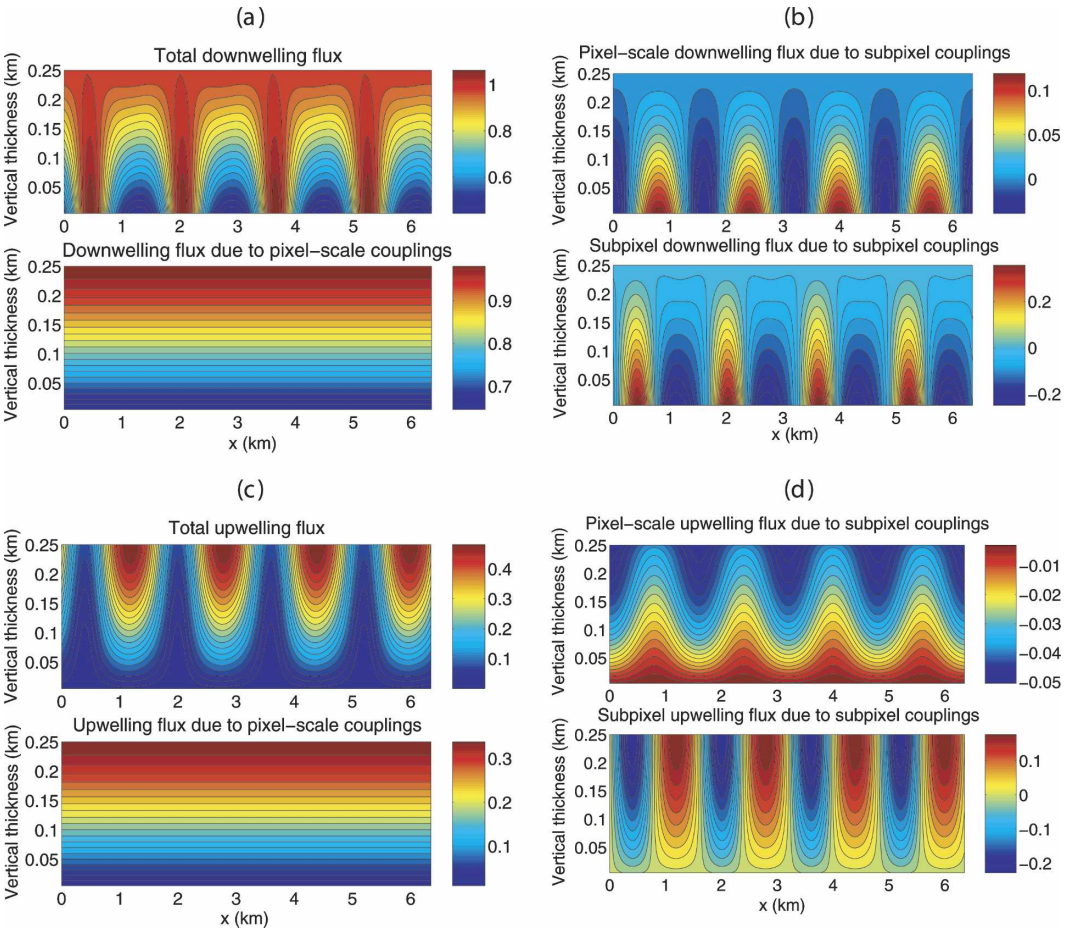

FIG. 8. Detailed fluxes inside the sine cloud; (a), (b) downwelling fluxes: [(a), top] $R_{\text{total}}^{\text{down}}$ and [(a), bottom] $R_{j_0}^{\text{down}}$; [(b), top] $R_{\psi\to j_0}^{\text{down}}$ and [(b), bottom] R_{ψ}^{down}. See text for the notations. (c), (d) Same as (a), (b) but for the upwelling fluxes. All fluxes are normalized.

cluded by the approximation of the cloud fields. It is interesting that in this representation, the sine cloud appears as a homogeneous plane-parallel cloud (Fig. 4a). Indeed, the eight scaling coefficients are all equal in this case, while the deviation of the original cloud from the plane-parallel approximation is totally represented by $\psi_{j_\psi=3}$. We note that this would not be the case if the same cloud is shifted by $\pm\pi/2$. The low resolution representation of the BC cloud exhibits a filtered curve with three relative maxima and minima (Fig. 4b) in which the central discontinuity is completely smoothed out. In the following subsections, we will examine how the radiation fields of these filtered clouds, unaffected by subpixel-scale couplings, differ from those of the original clouds.

b. Scale couplings in the radiative fluxes

Figures 8 and 10 show the different components of the fluxes and their sums at all locations inside the two clouds. Figures 8a,b and 10a,b show the downwelling (collimated + scattered) fluxes, and Figs. 8c,d and 10c,d the upwelling fluxes. The quantities $R_{j_0}^{\text{up/down}}$ are shown at the bottom of Figs. 8a,c and 10a,c, $R_{\psi\to j_0}^{\text{up/down}}$ and $R_{\psi}^{\text{up/down}}$ at the top and bottom of Figs. 8b,d and 10b,d, respectively, and the total fluxes $R_{\text{total}}^{\text{up/down}} = R_{j_0}^{\text{up/down}} + R_{\psi\to j_0}^{\text{up/down}} + R_{\psi}^{\text{up/down}}$ at the top of Figs. 8a,c and 10a,c. In interpreting these figures, it is important to pay attention to the color codes, which change from figure to figure.

1) SINE CLOUD

Since the low resolution representation of the sine cloud is a plane-parallel cloud, the radiative fluxes $R_{j_0}^{\text{up/down}}$ (bottom of Figs. 8a,c) appear as solutions to plane-parallel radiative transfer. The fluxes $R_{\psi\to j_0}^{\text{up/down}}$ (top of Figs. 8b,d) represent the contributions of subpixel-scale couplings to the pixel-scale fluxes. The numerical importance of these contributions seems small

TABLE 2. Fluxes leaving the sine cloud, in pixels 1 and 2 and at cloud scale. Pixel-scale and additional fluxes $R_{j_0}^{\text{up/down}n}$ and $R_{\psi\to j_0}^{\text{up/down}}$ are given, as well as their sums $R_{\text{total }j_0}^{\text{up/down}}$ and the contributions ($R_{\psi\to j_0}^{\text{up/down}}/R_{\text{total }j_0}^{\text{up/down}}$) in %.

	$R_{j_0}^{\text{up}}$	$R_{\psi\to j_0}^{\text{up}}$	$R_{\text{total }j_0}^{\text{up}}$	$(R_{\psi\to j_0}^{\text{up}}/R_{\text{total }j_0}^{\text{up}})$	$R_{j_0}^{\text{down}}$	$R_{\psi\to j_0}^{\text{down}}$	$R_{\text{total }j_0}^{\text{down}}$	$(R_{\psi\to j_0}^{\text{down}}/R_{\text{total }j_0}^{\text{down}})$
Pixel 1	0.354	−0.048	0.306	−15.0	0.646	−0.015	0.631	−2.3
Pixel 2	0.354	−0.040	0.314	−12.4	0.646	0.102	0.748	+13.7
Cloud scale	0.354	−0.044	0.310	−14.1	0.646	0.044	0.690	+6.4

as expected from the structure of the corresponding ECOs (cf. section 2c). The fluxes $R_{\psi\to j_0}^{\text{up/down}}$ exhibit the same four-cycle variation as in the cloud structure but slightly shifted. For the downwelling flux, $R_{\psi\to j_0}^{\text{down}}$ shows alternating positive and negative contributions in the high and low optical thickness regions. For the upwelling flux, $R_{\psi\to j_0}^{\text{up}}$ exhibits negative contributions through the whole cloud region, whose amplitude increases from the cloud base to the cloud top. The amplitude of $R_{\psi\to j_0}^{\text{up/down}}$ is more important in the low optical thickness regions, as are its corrections to $R_{j_0}^{\text{up/down}}$. These features tend to show that the main effect of $R_{\psi\to j_0}^{\text{up/down}}$ is to correct $R_{j_0}^{\text{up/down}}$ in the regions where the approximate cloud overestimates or underestimates the optical depth of the original cloud, even if this simple compensatory behavior is insufficient to explain the negative contribution of $R_{\psi\to j_0}^{\text{up}}$ in the high optical depth regions. An explanation of this last point lies in the horizontal photon transport as discussed below with reference to Table 2, and analyzed further in section 4c.

The subpixel-scale fluxes $R_{\psi}^{\text{up/down}}$ (bottom of Figs. 8b,d) exhibit again four-cycle variations that are also shifted, and numerically much larger than $R_{\psi\to j_0}^{\text{up/down}}$. The detailed variations of $R_{\text{total}}^{\text{up/down}}$ (top of Figs. 8a,c) are obtained by adding the above three fluxes. Their variations are, as expected, strongly correlated with variations in the cloud optical depth. The oblique angle of incidence of the collimated beam explains the slight asymmetry in their isocontours through the cloud layer.

Table 2 shows the components of the pixel-scale fluxes emerging at the cloud boundaries: $R_{j_0}^{\text{up/down}}$, $R_{\psi\to j_0}^{\text{up/down}}$, and their sums $R_{\text{total }j_0}^{\text{up/down}}$, in each approximation pixel and their averages at the outer scale. In the case of the sine cloud, radiation fields in odd (even) numbered pixels N°1, 3, 5, 7 (N°2, 4, 6, 8) are the same. Thus Table 2 gives only the results for pixels N°1 and 2. The variation of optical depth in odd/even pixels is shown in Fig. 9. As already described above, the flux $R_{\psi\to j_0}^{\text{up}}$ is everywhere negative, −0.048 and −0.040 in odd/even pixels, respectively. This leads to a relative contribution $R_{\psi\to j_0}^{\text{up}}/R_{\text{total }j_0}^{\text{up}}$ of −15.9% and −12.4%. The flux $R_{\psi\to j_0}^{\text{down}}$ is slightly negative in odd pixels (−0.015) and positive in even pixels (0.102), leading to a relative contribution $R_{\psi\to j_0}^{\text{down}}/R_{\text{total }j_0}^{\text{down}}$ of −2.3% and −13.7%. A more detailed analysis shows that the additional directly transmitted flux is everywhere positive (0.053 and 0.154 in odd/even pixels). In contrast, the additional scattered transmitted flux is everywhere negative (−0.068 and −0.051). Thus, the approximated calculation overestimates the scattered fields, and the sign of the additional pixel-scale scattered fluxes are negative for both the two hemispheres, as confirmed in Fig. 5. The evolution of $R_{\psi\to j_0}^{\text{up}}$ (Fig. 5b) shows how the plane-parallel bias, the well-known feature of the plane-parallel calculation (Cahalan et al. 1994a), varies with the order of scattering. Because the transmitted direct beam is underestimated and the transmitted scattered flux is overestimated, the two may compensate in the additional pixel-scale downwelling flux $R_{\psi\to j_0}^{\text{down}}$. While the domain average of $R_{\psi\to j_0}^{\text{up}}$ is still negative and large (−14.12%), the domain average of $R_{\psi\to j_0}^{\text{down}}$ is positive and smaller (+6.38%). Finally, the energy budget at the pixel scale $R_{\text{total }j_0}^{\text{up}} + R_{\text{total }j_0}^{\text{down}}$ shows total outgoing energy of 0.937 and 1.063 for pixels N°1 and 2, respectively. These features may be explained by shadowing and channeling effects (Davis and Marshak 2001) corresponding to a net photon transport from pixel N°1 to N°2. Because the approximated calculation corre-

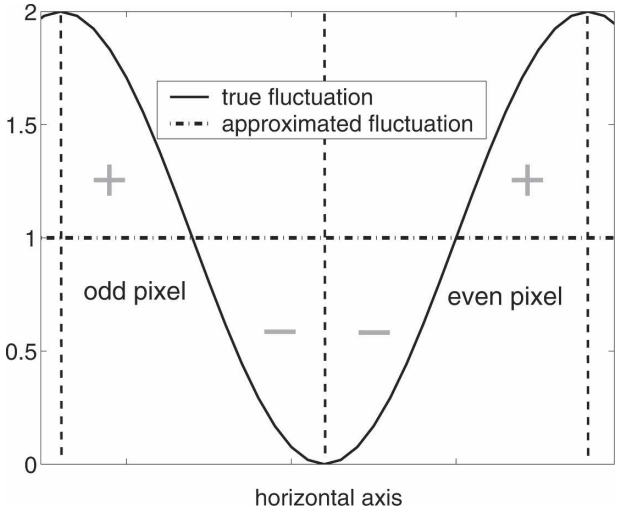

FIG. 9. Visualization of Meyer's approximation pixels and the true and approximated optical depth fluctuations for the sine cloud. The signs + and − indicate the presence of additional radiation sources, positive and negative, respectively.

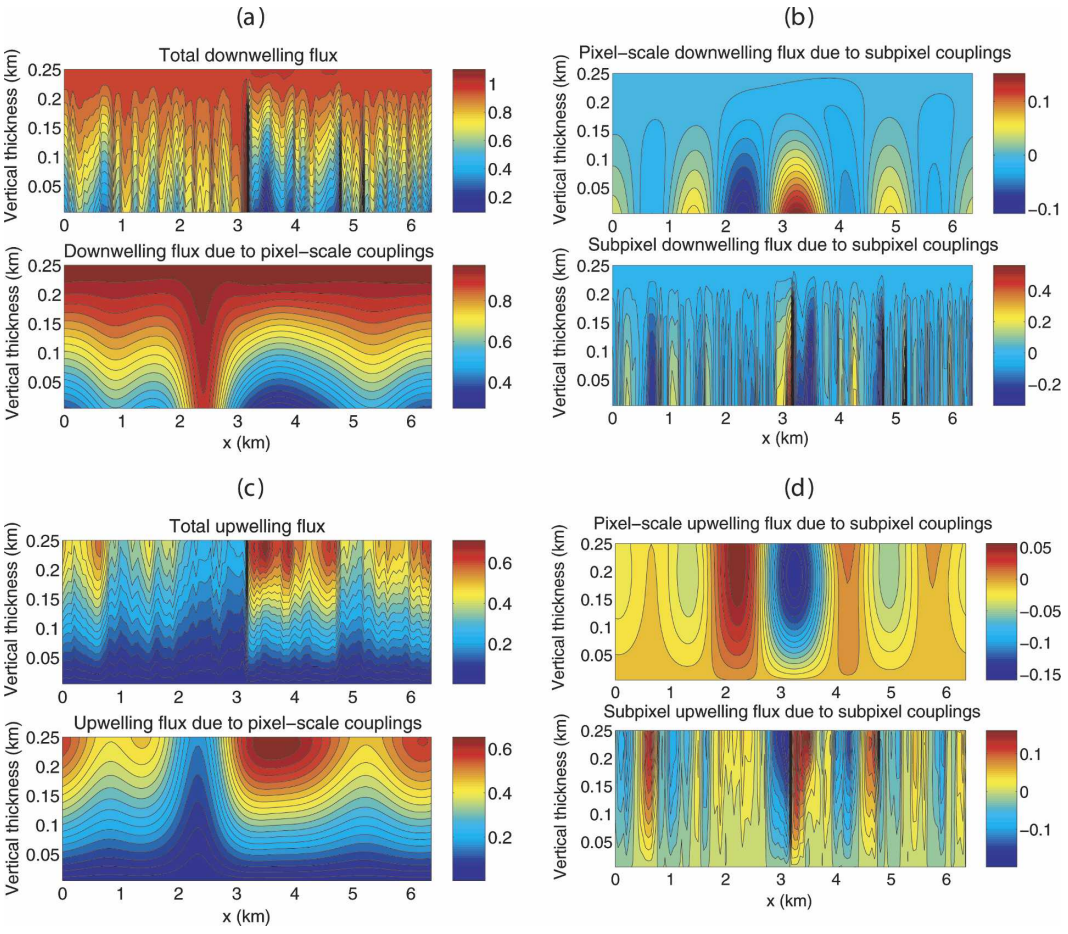

FIG. 10. As in Fig. 8 except for inside the BC cloud.

sponds to the plane-parallel assumption, these effects are only accounted by the subpixel contributions.

2) BC CLOUD

Figure 10 shows the same detailed variations of fluxes as Fig. 8, but for the BC cloud. Table 3 provides the radiation budget for the eight approximation pixels. Pixels N°2, 4, and 8, centered at 0.8, 2.4, and 5.6 km, respectively, correspond approximately to three minima in the optical thickness of the coarse BC cloud, while pixels N°1, 3, and 6 centered at 0, 1.6, and 4.0 km correspond to three maxima.

Radiative fluxes $R_{j_0}^{\text{up/down}}$ (bottom plots in Figs. 10a,c) represent the solution of the RTE for the approximated BC cloud by taking into account only the pixel-scale couplings. When we compute the sum $R_{j_0}^{\text{up}} + R_{j_0}^{\text{down}}$

TABLE 3. Fluxes leaving the BC cloud, in the eight approximation pixels and at cloud scale. Pixel-scale and additional fluxes $R_{j_0}^{\text{up/down}n}$ and $R_{\psi\to j_0}^{\text{up/down}}$ are given, as well as their sums $R_{\text{total } j_0}^{\text{up/down}}$ and the contributions $(R_{\psi\to j_0}^{\text{up/down}}/R_{\text{total } j_0}^{\text{up/down}})$ in %.

	$R_{j_0}^{\text{up}}$	$R_{\psi\to j_0}^{\text{up}}$	$R_{\text{total } j_0}^{\text{up}}$	$(R_{\psi\to j_0}^{\text{up}}/R_{\text{total } j_0}^{\text{up}})$	$R_{j_0}^{\text{down}}$	$R_{\psi\to j_0}^{\text{down}}$	$R_{\text{total } j_0}^{\text{down}}$	$(R_{\psi\to j_0}^{\text{down}}/R_{\text{total } j_0}^{\text{down}})$
Pixel 1	0.572	−0.013	0.559	−2.3	0.398	0.025	0.423	+5.9
Pixel 2	0.446	−0.021	0.425	−5.0	0.565	0.004	0.569	+0.7
Pixel 3	0.419	−0.006	0.413	−1.6	0.534	0.035	0.569	+6.2
Pixel 4	0.226	0.041	0.267	+15.4	0.828	−0.084	0.744	−11.2
Pixel 5	0.609	−0.135	0.474	−28.4	0.390	0.144	0.534	+27.1
Pixel 6	0.660	−0.003	0.657	−0.5	0.288	−0.013	0.275	−4.8
Pixel 7	0.514	−0.032	0.482	−6.7	0.467	0.044	0.511	+8.5
Pixel 8	0.507	−0.00	0.498	−1.7	0.516	−0.004	0.512	−0.8
Cloud scale	0.494	−0.022	0.472	−4.7	0.498	0.019	0.518	+3.7

from Table 3, we obtain 1.011, 1.054, and 1.023 for pixels N°2, 4, and 8, and 0.970, 0.953, and 0.948 for pixels N°1, 3, and 6. These values show clearly the pixel-scale channeling of the radiation energy due to pixel-scale couplings, from high into low optical depth regions; the channeling of downwelling flux for pixel N°4 is clearly shown at the bottom of Fig. 10a.

In the pixel-scale fluxes $R^{\mathrm{up/down}}_{\psi\to j_0}$ (top plots in Fig. 10b,d), the dominant features are those associated with the central discontinuity, but we can easily distinguish eight areas corresponding to the eight pixels. Their contributions are numerically larger for the BC cloud than for the sine cloud because of the larger excursions in the optical depth of the former. The downwelling flux $R^{\mathrm{down}}_{\psi\to j_0}$ shows very high negative and positive contributions around pixels N°4 and 5, respectively, which compensates for the excessive channeling observed at the bottom of Fig. 10a, but also accounts for the existence of very low optical depth in the original cloud at pixel N°5. The upwelling flux $R^{\mathrm{up}}_{\psi\to j_0}$ exhibits a slightly negative contribution through the entire cloud domain with high positive (negative) contributions around pixel N°4 (N°5). Here also, the principal contribution of $R^{\mathrm{up/down}}_{\psi\to j_0}$ seems to be the correction of $R^{\mathrm{up/down}}_{j_0}$ in the regions where the approximate cloud overestimates/underestimates the actual optical depth. The negative sign of $R^{\mathrm{up}}_{\psi\to j_0}$ in seven of the eight approximation pixels can be explained as in the sine cloud case. The flux $R^{\mathrm{up}}_{\psi\to j_0}$ is positive only in the fourth pixel N°4, inside which the approximated BC cloud underestimates everywhere the optical depth (see Fig. 4b between the abscissa 2.0 and 2.8 km).

The relative contributions $R^{\mathrm{up}}_{\psi\to j_0}/R^{\mathrm{up}}_{\mathrm{total}\,j_0}$ (see Table 3) are +15.4% and −28.4% for pixels N° 4 and 5, respectively, almost compensated by the relative contributions $R^{\mathrm{down}}_{\psi\to j_0}/R^{\mathrm{down}}_{\mathrm{total}\,j_0}$ of −11.2% and +27.1%. For other pixels, the subpixel contributions remain relatively small (below ±5%). At the cloud scale, these contributions nearly compensate (+3.7% and −4.7%). The energy budget at the pixel scale is computed from Table 3: its value ranges from 0.982 to 1.011 for all the pixels except pixel N°6 (0.932). These values show that the budget at the pixel scale is better conserved in the BC cloud than in the sine cloud discussed above, which implies less net horizontal photon transport between neighboring pixels. Comparing now the pixel-scale channeling with or without subpixel contributions, we observe that the effects of $R^{\mathrm{up/down}}_{\psi\to j_0}$ is slightly to reduce the pixel-scale channeling due to pixel-scale couplings in pixels N°1, 2, 7, and 8, and significantly in pixels N°3 and 4. In these pixels, energy conservation changes from 0.953 and 1.054, respectively (values due to pixel-scale couplings only), to 0.982 and 1.011.

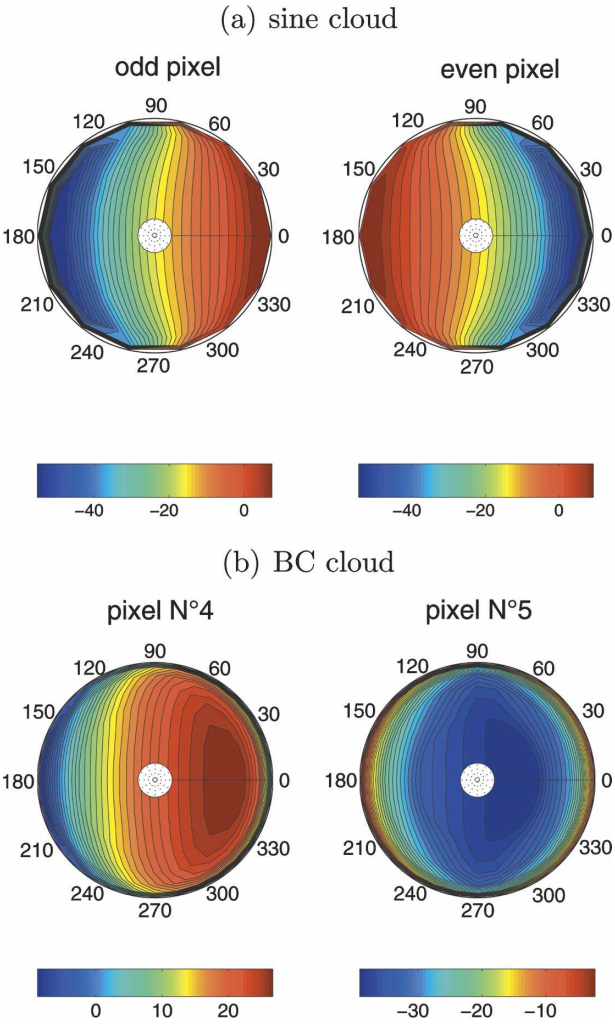

FIG. 11. Relative contributions (in %) of subpixel-scale inhomogeneities to pixel-scale outgoing upwelling radiances: (a) case of the sine cloud in (left) odd and (right) even pixels; (b) case of the BC cloud in the pixels N° (left) 4 and (right) 5.

The subpixel-scale fluxes $R^{\mathrm{up/down}}_{\psi}$ (bottom of Figs. 10b,d) exhibit rapidly fluctuating positive and negative contributions, reflecting the finescale fluctuations in the optical depth and are again numerically much larger than $R^{\mathrm{up/down}}_{\psi\to j_0}$. The variations of the total fluxes $R^{\mathrm{up/down}}_{\mathrm{total}}$ (top of Figs. 10a,c) follow well those of cloud optical depth, and exhibit the actual channeling of radiation at the center of the domain for $R^{\mathrm{down}}_{\mathrm{total}}$.

c. *Scale couplings in the radiance fields*

We examine how the 800-m pixel-scale radiances are affected by the contributions of scale couplings. We discuss here only the upwelling radiances at the cloud's top because such radiances would be remotely sensed by satellites to retrieve cloud parameters. In Fig. 11,

relative contributions $R^{up}_{\psi\to j_0}/R^{up}_{total\, j_0}$ (the same notation is used here for radiances as for fluxes in section 4b) are shown in a polar plot: the distance from the disk's center is given by $\sin\theta$ while the azimuthal angle φ follows the circumference of the circle.

1) SINE CLOUD

Figure 11a gives $R^{up}_{\psi\to j_0}/R^{up}_{total\, j_0}$ in the sine cloud case. Its variation is quasi parallel to the axis $\varphi = 90°$ and symmetrical with respect to the axis $\varphi = 0°$, a consequence of the cloud optical properties' independence of the y coordinate. Since the optical depth exhibits a symmetrical variation in odd and even pixels (Fig. 9), the two polar representations are near mirror images of each other. The maxima and minima of the relative contribution correspond to the largest zenith angles. For odd (even) numbered pixels, it varies from −56% (+10%) for the backward direction ($90° \le \varphi \le 270°$) to +8% (−55%) for the forward direction ($\varphi \le 90°$ and $\varphi \ge 270°$). These values show that contributions by subpixel scales is much larger for radiances than for fluxes, implying that the problem of subpixel cloud inhomogeneity is more serious in cloud parameter retrievals than in radiative flux computations.

Let us try to explain the variation in sign of the subpixel contributions $R^{up}_{\psi\to j_0}$, correction to the plane-parallel radiances $R^{up}_{j_0}$. The difference between the original and filtered optical depth inside the approximation pixels determines the sign of the additional radiation sources, as illustrated in Fig. 9. Additional sources are negative and positive where the plane-parallel approximation respectively overestimates and underestimates the optical depth. The magnitude of the negative sources is larger, because neglecting the smallest values of the optical depth instead of the largest leads to larger errors. These additional sources propagate relatively freely toward areas where the optical depth is low, that is, the central part of Fig. 9. Positive additional sources (exterior parts of Fig. 9) propagate obliquely and yield positive contributions $R^{up}_{\psi\to j_0}$ in forward (backward) directions for odd (even) pixels at large zenith angles (see Fig. 11a). Negative additional sources propagate around nadir and illuminate obliquely the central part of the neighbor pixel, yielding globally negative contribution $R^{up}_{\psi\to j_0}$ that can become large in backward (forward) directions for odd (even) pixel (see Fig. 11a). At cloud scale, the subpixel contributions to the upwelling radiances are negative for all the directions, mostly between and −23% and −13%.

This short analysis allows us to understand the subpixel contributions to the pixel-scale reflected field, its magnitude and signs. Plane-parallel errors come mostly from the neglect of low optical depth regions, that leads to additional negative radiation sources that propagate easily through these regions and determine the negative sign of the additional pixel-scale albedo (see Table 2).

2) BC CLOUD

In this case, an important observation is that the radiances $R^{up}_{j_0}$ of the approximated cloud vary with the pixels in contrast to the sine cloud. The quantity $R^{up}_{\psi\to j_0}$ is the correction to these coarse cloud radiances. This correction changes from one pixel to another and is dictated by the effects of its neighboring pixels and its subpixel-scale internal variation. Figure 11b shows for example the relative contribution $R^{up}_{\psi\to j_0}/R^{up}_{total\, j_0}$ in pixels N°4 and 5. In pixel N°4, the relative subpixel contribution to the radiances ranges from −9% to +27% while varying from −40% to −2% in pixel N°5. We do not discuss here these sign variations or values, as that would require a very detailed analysis, but only check the consistency between these relative contributions and the additional pixel-scale fluxes given in Table 3. At the cloud scale, the subpixel contributions nearly cancel and span the range between −7% and −1%.

5. Summary and conclusions

The objectives of this two-part study were to analyze scale coupling in radiative transfer through inhomogeneous media, and to improve our understanding of the effects of cloud inhomogeneity in radiation modeling. Our approach consisted in applying a multiresolution (MR) transformation to the radiative transfer equation (RTE), thus providing a theoretical framework that defines the notion of scale coupling in radiative transfer problems. Part I developed this framework that yielded two new RTEs applicable at the pixel scale and subpixel scales. A key property of the pixel-scale RTE is that it reveals that the radiation field is decomposable into a component due to the radiative transfer through a cloud approximated at the pixel scale, and a component caused by additional internal radiation sources due to scale couplings.

The formalism we developed not only introduces a new way to compute the 3D radiative transfer, but also evaluates locally the additional sources originating from scale couplings at the scale of each approximation pixel of the entire cloud field. This represents a significant advancement over the Fourier approach described earlier, because the latter describes cloud inhomogeneities with Fourier coefficients depending on the cloud fluctuation over the domain scale and thus can quantify the effects of cloud multiscale inhomogeneities only at that (domain) scale.

Part II calculates the numerical solution of this new set of equations and analyses the effects of scale couplings on the radiation fields. Solving numerically the MR RTEs raises immediately the issue of selecting a specific MR system for this purpose. After discussing the desirable properties such a MR system should have, we decided to use Meyer's system for this study, in spite of its shortcomings. We then investigated the structure of Meyer's connection coefficients for the product, which defines all potential scale couplings in Meyer's MR RTEs. Scale couplings that contribute in a given radiative transfer problem are represented by the effective coupling operators (ECOs). The ECOs of the sine and BC clouds exhibit significant differences in the scale couplings.

Fluxes and radiances computed with the MR radiative transfer code WaveNum were in good agreement with those calculated using SHDOM and a Monte Carlo code. WaveNum maintained its accuracy, even in the presence of some numerical noise introduced by Gibbs phenomenon.

A useful and interesting feature of WaveNum is its ability to separate the radiation field into three different components: 1) $R_{j_0}^{\text{up/down}}$, the solution of the pixel-scale RTE without the additional internal source terms, that is, for the approximated cloud; (2) $R_{\psi\to j_0}^{\text{up/down}}$, the additional pixel-scale radiation field due to the additional internal radiation sources; and 3) $R_{\psi}^{\text{up/down}}$, the solution of the subpixel-scale RTE with the additional internal source terms.

Thus, the total unbiased pixel-scale radiation field $R_{\text{total}\,j_0}^{\text{up/down}}$ is composed of $R_{j_0}^{\text{up/down}}$ and $R_{\psi\to j_0}^{\text{up/down}}$. The third component $R_{\psi}^{\text{up/down}}$, developed using wavelets, fluctuates rapidly and is filtered out when averaged over a pixel. For our two synthetic clouds, contributions of $R_{\psi\to j_0}^{\text{up/down}}$ to the pixel-scale radiation field $R_{\text{total}_0}^{\text{up/down}}$ reach $\pm 30\%$ for the fluxes, and -55% for the radiances. This shows clearly that the contributions of subpixel-scale couplings to the radiation field at the pixel scale are, in many cases, too large to be simply ignored.

For the conservative scattering cases studied here, the main contribution of cloud subpixel fluctuations at the pixel scale and the cloud domain scale is to redistribute energy between reflected and transmitted fluxes. Moreover, the energy budget at the pixel scale is modified, a consequence of additional net horizontal photon transport. Using the sine cloud, we have analyzed and explained the well-known plane-parallel albedo bias. Using the BC cloud, we have shown that the effect of $R_{\psi}^{\text{up/down}}$, is surprisingly to reduce in most of the pixels the pixel-scale channeling due to pixel-scale couplings. More generally, $R_{\psi\to j_0}^{\text{up/down}}$ seems to reflect qualitatively how the difference between the original and filtered optical depth field varies within each approximation pixel. We have observed that the larger contributions are due to the neglect of low optical depth regions within the pixel. However, it is difficult to generalize further from these observations. The importance of scale couplings can be quantified only after integrating the equations over the cloud domain. The ECOs however are the fundamental mechanism of local-scale couplings. An important theoretical issue is to develop a methodology for the analysis of global-scale couplings.

This formalism allows for the analysis of scale couplings and the computation of fluxes and radiances at the pixel scale, thus gaining new insights into the radiative transfer in inhomogeneous media. It may also provide a theoretical framework to simplify and approximate radiative transfer problems in inhomogeneous media, keeping a desired accuracy. Such approximations are useful to remote sensing applications. We have hope that future studies using the MR approach will allow us to analyze, for example, the effects of thresholding ECOs to enhance the sparsity of their matrix representation and to deduce which couplings are dominant, and thus which aspects of the cloud variability are important radiatively. The methodology provided here is powerful for studying 3D radiative transfer, which can yield depth of understanding not possible by just comparing independent pixel approximation (IPA) and 3D radiative transfer results.

For the WaveNum code to become practical, extensive code development will be required in a more powerful programming language. The results computed in this paper were all derived using MATLAB. To obtain computational efficiency, convergence can be accelerated by using variable step size other numerical integration schemes as well as extrapolation techniques. The formulation can be recast in an eigenvalue problem or solved by the doubling–adding approach. Numerical efficiency can also be realized by thresholding the values of the connection coefficients thus increasing the sparsity of their matrix representation. Finally, the methodology described can yield useful parameterizations of the effects of subgrid-scale cloud variability on larger scales. These are goals of future studies.

Acknowledgments. This work is based on the Ph.D. dissertation of Nicolas Ferlay, financed by the French Minister of Research, and was supported by the Japanese Space Agency (NASDA) Project GLI/ADEOSII Grant 14GRF001 and partially by the NASA Project RSP-000-0167. The authors thank Céline Cornet and

Frédéric Szczap for their SHDOM and Monte Carlo simulations.

REFERENCES

Abry, P., 1996: *Ondelettes et Turbulences: Multirésolution, Algorithmes de Décomposition, Invariance D'échelle et Signaux de Pression.* Diderot Editeur, Arts et Sciences, 290 pp.

Cahalan, R. F., 1994: Bounded cascade clouds: Albedo and effective thickness. *Nonlinear Processes Geophys.,* **1,** 156–167.

——, W. Ridgway, W. J. Wiscombe, and T. L. Bell, 1994a: The albedo of fractal stratocumulus clouds. *J. Atmos. Sci.,* **51,** 2434–2455.

——, ——, ——, and ——, 1994b: Independent pixel and Monte Carlo estimates of stratocumulus albedo. *J. Atmos. Sci.,* **51,** 3776–3790.

Cess, R. D., and Coauthors, 1990: Intercomparison and interpretation of climate feedback processes in 19 atmospheric general circulation models. *J. Geophys. Res.,* **95,** 16 601–16 615.

Cornet, C., H. Isaka, B. Guillemet, and F. Szczap, 2004: Neural network retrieval of cloud parameters of inhomogeneous clouds from multispectral and multiscale radiance data: Feasibility study. *J. Geophys. Res.,* **109,** D12203, doi:10.1029/2003JD004186.

Davis, A. B., and A. Marshak, 2001: Multiple scattering in clouds: Insights from three-dimensional diffusion/p1 theory. *Nucl. Sci. Eng.,* **137,** 251–280.

——, ——, W. Wiscombe, and R. Cahalan, 1996: Scale invariance of liquid water distributions in marine stratocumulus. Part I: Spectral properties and stationarity issues. *J. Atmos. Sci.,* **53,** 1538–1558.

Evans, K. F., 1998: The Spherical Harmonics Discrete Ordinate Method for three-dimensional atmospheric radiative transfer. *J. Atmos. Sci.,* **55,** 429–446.

Faure, T., H. Isaka, and B. Guillemet, 2001: Neural network retrieval of cloud parameters of inhomogeneous and fractional clouds; Feasibility study. *Remote Sens. Environ.,* **77,** 123–138.

——, ——, and ——, 2002: Neural network retrieval of cloud parameters from high resolution multispectral radiometric data; A feasibility study. *Remote Sens. Environ.,* **80,** 285–296.

Ferlay, N., and H. Isaka, 2006: Multiresolution analysis of radiative transfer through inhomogeneous media. Part I: Theoretical development. *J. Atmos. Sci.,* **63,** 1200–1212.

Gabriel, P. M., S.-C. Tsay, and G. L. Stephens, 1993: A Fourier–Ricatti approach to radiative transfer. Part I: Foundations. *J. Atmos. Sci.,* **50,** 3125–3147.

Jerri, A. J., 1998: *The Gibbs Phenomenon in Fourier Analysis, Splines and Wavelet Approximations.* Vol. 446, *Mathematics and its Applications,* Kluwer Academic, 336 pp.

Kolaczyk, E. D., 1994: Wavelet methods for the inversion of certain homogeneous linear operators in the presence of noisy data. Ph.D. thesis, Stanford University, 152 pp.

Marchuk, G. I., G. A. Mikhailov, M. A. Nazaraliev, R. A. Darbinjan, B. A. Kargin, and B. S. Elepov, 1980: *The Monte Carlo Methods in Atmospheric Optics.* Springer-Verlag, 208 pp.

——, A. Davis, R. F. Cahalan, and W. Wiscombe, 1994: Bounded cascade model as nonstationary multifractals. *Phys. Rev. E,* **49** (1), 48–69.

——, ——, W. Wiscombe, and G. Titov, 1995: The verisimilitude of the independent pixel approximation used in cloud remote sensing. *Remote Sens. Environ.,* **52,** 71–78.

McCormick, K., and R. O. J. Wells, 1994: Wavelet calculus and finite difference operators. *Math. Comput.,* **63,** 155–173.

Meyer, Y., 1990: *Ondelettes et Opérateurs.* Hermann, 215 pp.

Resnikoff, H. L., and R. O. Wells, 1998: *Wavelet Analysis: The Scalable Structure of Information.* Springer-Verlag, 435 pp.

Stephens, G. L., 1988a: Radiative transfer through arbitrarily shaped optical media. Part I: A general method of solution. *J. Atmos. Sci.,* **45,** 1818–1836.

——, 1988b: Radiative transfer through arbitrarily shaped optical media. Part II: Group theory and simple closures. *J. Atmos. Sci.,* **45,** 1837–1848.

Várnai, T., and A. Marshak, 2001: Statistical analysis of the uncertainties in cloud optical depth retrievals caused by three-dimensional radiative effects. *J. Atmos. Sci.,* **58,** 1540–1548.

Walter, G. G., and X. Shen, 2001: *Wavelets and Other Orthogonal Systems*. 2d ed., Studies in Advanced Mathematics, Chapman and Hall/CRC, 370 pp.